

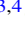







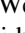

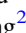
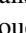

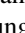

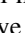



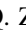
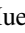
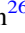


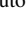




Magnetic Fields in Massive Star-forming Regions (MagMaR). IV. Tracing the Magnetic Fields in the O-type Protostellar System IRAS 16547–4247

Luis A. Zapata¹ , Manuel Fernández-López² , Patricio Sanhueza^{3,4} , Josep M. Girart⁵ , Luis F. Rodríguez¹ , Paulo Cortés^{6,7} , Patrick Koch⁸ , Maria T. Beltrán⁹ , Kate Pattle¹⁰ , Henrik Beuther¹¹ , Piyali Saha³ , Wenyu Jiao^{12,13} , Fengwei Xu^{12,14,15} , Xing Walker Lu¹⁶ , Fernando Olguin¹⁷ , Shanghuo Li¹¹ , Ian W. Stephens¹⁸ , Ji-hyun Kang¹⁹ , Yu Cheng²⁰ , Spandan Choudhury²¹ , Kaho Morii^{3,22} , Eun Jung Chung²³ , Jia-Wei Wang¹⁷ , Jihye Hwang²⁴ , A-Ran Lyo²⁴ , Q. Zhang²⁵ , and Hwei-Ru Vivien Chen²⁶ 

¹ Instituto de Radioastronomía y Astrofísica, Universidad Nacional Autónoma de México, P.O. Box 3-72, 58090, Morelia, Michoacán, Mexico; lzapata@ira.unam.mx

² Instituto Argentino de Radioastronomía (CCT-La Plata, CONICET; CICPBA), C.C. No. 5, 1894, Villa Elisa, Buenos Aires, Argentina

³ National Astronomical Observatory of Japan, National Institutes of Natural Sciences, 2-21-1 Osawa, Mitaka, Tokyo 181-8588, Japan

⁴ Department of Astronomical Science, SOKENDAI (The Graduate University for Advanced Studies), 2-21-1 Osawa, Mitaka, Tokyo 181-8588, Japan

⁵ Institut d'Estudis Espacials de Catalunya (IEEC), c/Gran Capita, 2-4, E-08034 Barcelona, Catalonia, Spain

⁶ Joint ALMA Observatory, Alonso de Córdova 3107, Vitacura, Santiago, Chile

⁷ National Radio Astronomy Observatory, 520 Edgemont Road, Charlottesville, VA 22903, USA

⁸ Institute of Astronomy and Astrophysics, Academia Sinica, No. 1, Sec. 4, Roosevelt Road, Taipei 10617, Taiwan

⁹ INAF-Osservatorio Astrofisico di Arcetri, Largo E. Fermi 5, I-50125 Firenze, Italy

¹⁰ Department of Physics and Astronomy, University College London, Gower Street, London WC1E 6BT, UK

¹¹ Max Planck Institute for Astronomy, Königstuhl 17, D-69117 Heidelberg, Germany

¹² Department of Astronomy, School of Physics, Peking University, Beijing 100871, People's Republic of China

¹³ Kavli Institute for Astronomy and Astrophysics, Peking University, Haidian District, Beijing 100871, People's Republic of China

¹⁴ I. Physikalisches Institut, Universität zu Köln, Zùlpicher Str. 77, D-50937 Köln, Germany

¹⁵ Kavli Institute for Astronomy and Astrophysics, Peking University, Beijing 100871, People's Republic of China

¹⁶ Shanghai Astronomical Observatory, Chinese Academy of Sciences, 80 Nandan Road, Xuhui, Shanghai 200030, People's Republic of China

¹⁷ Institute of Astronomy and Department of Physics, National Tsing Hua University, Hsinchu 30013, Taiwan

¹⁸ Department of Earth, Environment, and Physics, Worcester State University, Worcester, MA 01602, USA

¹⁹ Korea Astronomy and Space Science Institute, 776 Daedeok-daero, Yuseong, Daejeon 34055, Republic of Korea

²⁰ National Astronomical Observatory of Japan, 2-21-1 Osawa, Mitaka, Tokyo 181-8588, Japan

²¹ Korea Astronomy and Space Science Institute, 776 Daedeok-daero Yuseong-gu, Daejeon 34055, Republic of Korea

²² Department of Astronomy, Graduate School of Science, The University of Tokyo, 7-3-1 Hongo, Bunkyo-ku, Tokyo 113-0033, Japan

²³ Korea Astronomy and Space Science Institute, 776 Daedeokdae-ro, Yuseong-gu, Daejeon, Republic of Korea

²⁴ Korea Astronomy and Space Science Institute (KASI), 776 Daedeokdae-ro, Yuseong-gu, Daejeon 34055, Republic of Korea

²⁵ Center for Astrophysics, Harvard & Smithsonian, 60 Garden Street, Cambridge, MA 02138, USA

²⁶ Institute of Astronomy and Department of Physics, National Tsing Hua University, Hsinchu 300044, Taiwan

Received 2024 May 17; revised 2024 August 13; accepted 2024 August 14; published 2024 October 16

Abstract


The formation of the massive stars, and in particular, the role that the magnetic fields play in their early evolutionary phase is still far from being completely understood. Here, we present the Atacama Large Millimeter/submillimeter Array 1.2 mm full polarized continuum and $\text{H}^{13}\text{CO}^+(3-2)$, $\text{CS}(5-4)$, and $\text{HN}^{13}\text{C}(3-2)$ line observations with a high angular resolution (~ 0.7 or 1100 au). In the 1.2 mm continuum emission, we reveal a dusty envelope surrounding the massive protostars, IRAS16547-E and IRAS16547-W, with dimensions of $\sim 10,000$ au. This envelope has a biconical structure likely carved by the powerful thermal radio jet present in region. The magnetic field vectors follow very well the biconical envelope. The polarization fraction is $\sim 2.0\%$ in this region. Some of these vectors seem to converge to IRAS 16547-E and IRAS 16547-W, the most massive protostars. Moreover, the velocity fields revealed from the spectral lines $\text{H}^{13}\text{CO}^+(3-2)$ and $\text{HN}^{13}\text{C}(3-2)$ show velocity gradients with a good correspondence with the magnetic fields, which maybe are tracing the cavities of molecular outflows or maybe infalling in some parts. We derived a magnetic field strength in some filamentary regions that goes from 2 to 6.1 mG. We also find that the $\text{CS}(5-4)$ molecular line emission reveals multiple outflow cavities or bow shocks with different orientations, some of which seem to follow the NW–SE radio thermal jet.

Unified Astronomy Thesaurus concepts: [Star formation \(1569\)](#)

1. Introduction

One of the key ingredients influencing the formation of the massive stars ($M_* > 10 M_\odot$) is very likely the magnetic field. The magnetic fields can regulate or even prevent the infall of

material toward the nascent massive stars (C. L. H. Hull & Q. Zhang 2019). At the moment, there is increasing evidence, for example, that the magnetic fields drive the energetic outflows and jets that emanate from protostars, which remove angular momentum from the system, thereby allowing the material to be transported directly onto the central protostar (R. D. Blandford & D. G. Payne 1982; C.-F. Lee et al. 2017; A. de Valon et al. 2020; R. Launhardt et al. 2023; J. A. López-Vázquez et al. 2023). However, the magnetic fields in most of

 Original content from this work may be used under the terms of the [Creative Commons Attribution 4.0 licence](#). Any further distribution of this work must maintain attribution to the author(s) and the title of the work, journal citation and DOI.

the massive star-forming regions are not well understood due to the large distances to these regions and their scarcity. Recently, thanks to the new sensitive and superb angular resolution observations of the thermal dust polarization (using, e.g., Atacama Large Millimeter/submillimeter Array, ALMA; the Jansky Very Large Array, or the Submillimeter Array), there has been a surge of new cases where the morphology and the strength are starting to be known with a fascinating clarity (M. T. Beltrán et al. 2019; H. Beuther et al. 2020; J. Liu et al. 2020; P. C. Cortés et al. 2021, 2024; M. Fernández-López et al. 2021; A. Palau et al. 2021; P. Sanhueza et al. 2021; P. M. Koch et al. 2022; J. Liu et al. 2023; K. Pattle et al. 2023; P. Saha et al. 2024).

For example, in the cases of the massive star-forming regions IRAS 18089–1732, G327.3, and W51 (in several cores), it has been proposed that the magnetic fields are tracing spiral-like accreting structures mapped in the 1.2 mm continuum emission arising from thermal dust and the molecular line emission (H. Beuther et al. 2020; P. Sanhueza et al. 2021; P. M. Koch et al. 2022). In all cases, the magnetic field morphology suggests that the angular momentum is high enough to twist the magnetic field lines, and the material can infall to the forming massive protostars.

Embedded in a massive dusty core with an estimated mass of $1.3 \times 10^3 M_{\odot}$ is found the luminous (with a bolometric luminosity of $6.2 \times 10^4 L_{\odot}$) infrared source IRAS 16547–4247 (G. Garay et al. 2003). This massive source is located at a distance of 2.9 ± 0.6 kpc (L. F. Rodríguez et al. 2008) and is powering one of the radio thermal jets related to a star-forming region (see also the case of DG Tau; L. F. Rodríguez et al. 2012). The radio thermal jet has a NW–SE orientation (L. F. Rodríguez et al. 2008; R. Franco-Hernández et al. 2009) and is part of an energetic molecular outflow traced by the CH_3OH , CO , and H_2 thermal emission (K. J. Brooks et al. 2003; G. Garay et al. 2007; A. E. Higuchi et al. 2015). In the middle of IRAS 16547–4247, there are two massive and compact (~ 500 au) rotating circumstellar disks reported recently, IRAS 16547-Ea and IRAS 16547-Eb (L. A. Zapata et al. 2019; K. E. I. Tanaka et al. 2020). One of these disks, IRAS 16547-Ea, is energizing the ionized free-free thermal jet and the molecular outflow (K. E. I. Tanaka et al. 2020). From the kinematics of the circumbinary disk that surrounds both compact disks (L. A. Zapata et al. 2019), the estimated mass for the central objects (the binary system) is around $25 \pm 3 M_{\odot}$, resulting in true O-type protostars (L. A. Zapata et al. 2019).

In this study, we present 1.2 mm dust polarization and molecular line ALMA observations of the rotating and massive hot molecular core embedded in the high-mass star-forming region IRAS 16547–4247. These observations reveal for the first time the detail structure of the magnetic fields associated with the dust and line emission from the envelope surrounding IRAS 16547–4247 (throughout our study we also refer to this source as IRAS 16547).

2. Observations

ALMA observations of IRAS 16547–4247 were undertaken on 2018 December under the program 2017.1.00101.S with PI: P. Sanhueza. At that time, the array included 45 antennas with a diameter of only 12 m and covering baselines from 15 to 783 m (12 to 652 $k\lambda$). The observations were pointed at the phase center $\alpha_{J2000.0} = 16^{\text{h}}58^{\text{m}}17^{\text{s}}.11$ and $\delta_{J2000.0} = -42^{\circ}52'07''.06$. The thermal dust and molecular gas emission in the Stokes I , Q ,

U , and V from IRAS 16547–4247 were covered with a single pointing with an FWHM of $22''.7$. Henceforth, we only consider the continuum sources and the polarization vectors inside of the FWHM as real. The largest angular scale that is recovered by these observations is $6''.3$. The total on-source integration time was 45 minutes.

The weather conditions during the observations were considerably good with an average precipitable water vapor of about 1.9 mm. The phase rms was only $19^{\circ}.8$. The atmospheric phase oscillation was reduced by the simultaneous observation of the 183 GHz water line with water vapor radiometers. Quasars J1751+0939, J1517–2422, and J1733–3722 were used to perform the bandpass calibration, the gain/atmospheric fluctuations, and the flux amplitude calibration. Some of the quasar scans were repeated for different calibrations.

The ALMA digital correlator was configured with five spectral windows (SPWs) intended to detect different molecular species in these millimeter wave bands and the adjacent continuum. Three SPWs were centered at rest frequencies of 243.518, 245.518, and 257.521 GHz and have a bandwidth of 1.875 GHz with a number of channels 1920, which gives a channel spacing of 976.5 kHz or 1.195 km s^{-1} . In order to construct the millimeter continuum emission for IRAS 16547–4247, we only used free-line channels in the SPWs. The rest of the SPWs were centered to detect the $\text{H}^{13}\text{CO}^+(3-2)$ and the $\text{HN}^{13}\text{C}(3-2)$ spectral lines (at rest frequencies of 260.25554 GHz and 261.26331 GHz, respectively) with a channel spacing of 0.281 km s^{-1} or 243.7 kHz. We also detected the spectral line $\text{CS}(5-4)$ at a rest frequency of 244.93555 GHz. The CS molecule is a high-density and classical outflow tracer (P. Sanhueza et al. 2010). The bulk of thermal emission only from these three spectral lines are discussed in this study.

The ALMA data were calibrated, analyzed, and imaged in a standard manner using Common Astronomy Software Applications (CASA) VERSION 5.4.0–68 (CASA Team et al. 2022). The resulting images were Fourier transformed, deconvolved, and restored using the CASA TCLEAN task. The resulting rms noise for the continuum image of the Stokes I is $0.2 \text{ mJy beam}^{-1}$ with a synthesized beam of $0''.44 \times 0''.39''$ and a position angle (PA) of $-83^{\circ}.1$. As in other cases (see L. A. Zapata et al. 2023), the rms noise is higher than the theoretical (which is about $0.05 \text{ mJy beam}^{-1}$). This is likely due to the strong millimeter continuum source localized in IRAS 16547–4247, which did not allow us to reach the theoretical rms noises. Contrary to the Stokes I , for the Stokes Q , U , and V images, the rms noise level is $0.05 \text{ mJy beam}^{-1}$, very close to the theoretical value. We construct the images of the debiased linear polarized intensity ($\sqrt{Q^2 + U^2} - 0.5[dQ^2 + dU^2]$), the linear debiased polarization fraction ($\sqrt{Q^2 + U^2}/I$), and the electric vector PA ($0.5\text{arctan}(U/Q)$), and they are present in Figures 1 and 2. The resulting rms noise for the line images in Stokes I is 3 mJy beam^{-1} per channel spacing with a synthesized beam of $0''.36 \times 0''.32$ and a PA of $-88^{\circ}.1$. We obtained values similar to the ALMA theoretical rms noise for the spectral line images.

Phase self-calibration (using interval solutions that included infinite, 60 s and 15 s) was made using the continuum (Stokes I) as a model. The spectral line channels were then corrected with the acquired solutions. The improvement in the continuum rms noise was almost a factor of 10 for the continuum and 3 for the line emission.

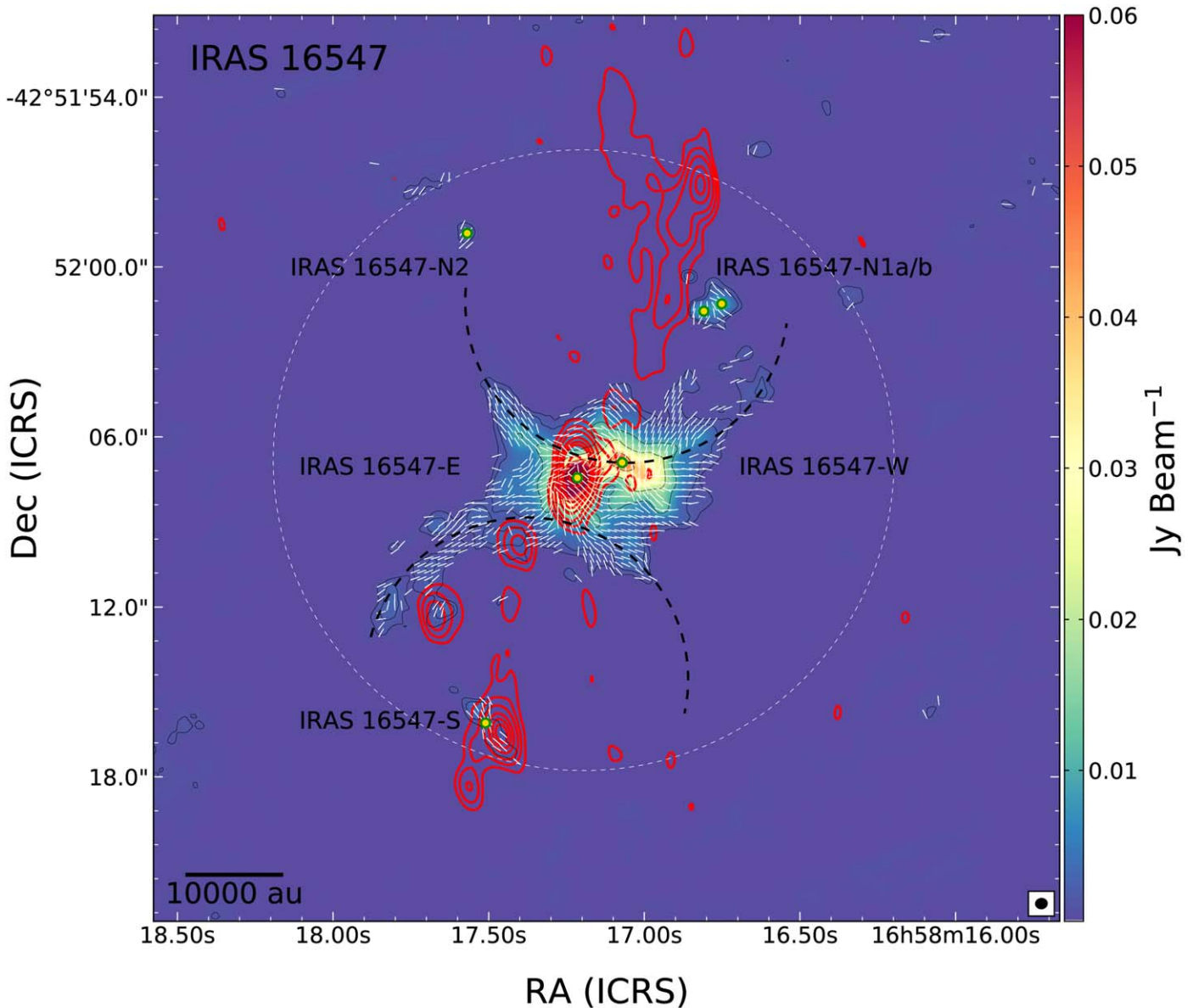


Figure 1. ALMA magnetic field vectors overlaid onto the resulting 1.2 mm continuum emission (Stokes I) from IRAS 16547–4247. The white vector segments trace the polarization percentage. The vector segment is displayed more or less per every beam, using only data with a 2σ cut in the debiasing process. The black contours are from $-0.5, 0.5, 1, 5, 10, 20, 40,$ and 60 times $0.2 \text{ mJy beam}^{-1}$ the rms noise of the image. The red contours are from $-5, 5, 10, 20, 40, 60, 80,$ and 180 times the rms noise of the Very Large Array (VLA) 3.6 cm continuum emission, which is $20 \mu\text{Jy beam}^{-1}$. The 3.6 cm continuum emission delineates the radio thermal jet with a NW–SE orientation reported by G. Garay et al. (2003) and L. F. Rodríguez et al. (2008). The synthesized beam (half-power contour) of the ALMA continuum image is shown in the bottom right corner. The scale bar on the right represents the peak flux of the ALMA 1.2 mm continuum emission. The dashed lines trace more or less the biconical dusty envelope revealed in this study. The white circle traces the primary beam or the FWHM of $22''.7$. The yellow dots trace the positions of the sources reported in Table 1.

3. Results and Discussion

3.1. ALMA Polarization Observations of IRAS 16547–4247

In Figure 1, we show one of the main results of this study, the inferred structure of the magnetic fields (white vectors) plotted on the 1.2 mm continuum emission from IRAS 16547–4247. In order to compute the magnetic field orientations, we are assuming that these structures are orthogonal to the linear polarization orientations of the electric vector PAs, a result from grains aligned by radiative torques to precess around the magnetic field direction (B-RAT alignment; T. Hoang & A. Lazarian 2008). Both the magnetic field orientations (vectors) and the 1.2 mm continuum emission (black contours) in IRAS 16547–4247 are arising from six continuum sources with physical parameters described in

Table 1. The faintest source, IRAS 16547N2, is at a 10σ level. The strongest sources of 1.2 mm continuum emission are associated with IRAS 16547-E and IRAS 16547-W. IRAS 16547-E is in addition related to a powerful radio free-free thermal jet (in red contours in Figure 1) with a NW–SE orientation that is emanating from one of the compact circumstellar disks called IRAS 16547-Ea and surrounds a true young O-type protostar (K. E. I. Tanaka et al. 2020). For the case of IRAS 16547-W, this source is also associated with hot molecular emission from complex organic molecules as revealed in Figure 2 of L. A. Zapata et al. (2019). This millimeter continuum source could also be related to a massive protostar (R. Franco-Hernández et al. 2009; L. A. Zapata et al. 2019). The present ALMA observations are sensitive to larger scales ($\sim 6''.3$),

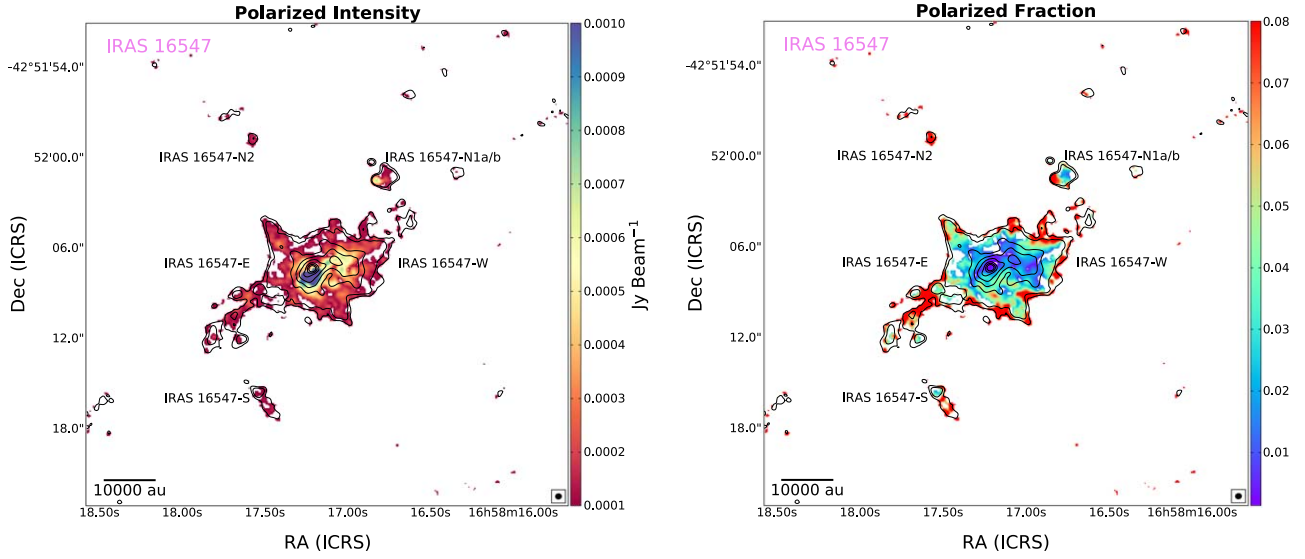


Figure 2. Left panel: ALMA polarization intensity map overlaid with the 1.2 mm continuum emission from IRAS 16547–4247. Right panel: same as the left panel but showing the ALMA Polarization Fraction. In both panels, the black contours are from $-0.5, 0.5, 1, 5, 10, 20, 40,$ and 60 times $0.2 \text{ mJy beam}^{-1}$ the rms noise of the image. The synthesized beam (half-power contour) of the ALMA continuum image is shown in the bottom right corner. The scale bar on the right represents the debiased polarization intensity and polarization fraction. These maps were constructed with a threshold of 2σ for the polarization.

Table 1
Physical Parameters of the 1.2 mm Continuum Sources

Source	Position		Deconvolved Size			Flux		Mass (M_{\odot})
	α_{2000} (h m s)	δ_{2000} (deg arcmin arcsec)	θ_{maj} (mas)	θ_{min} (mas)	PA (deg)	Peak (mJy beam $^{-1}$)	Integrated (mJy)	
IRAS 16547N1a	16 58 16''765 \pm 0''02	−42 52 01''37 \pm 0''01	830 \pm 70	550 \pm 50	116 \pm 10	9.5 \pm 0.5	34.5 \pm 2	1.4 (50 K)
IRAS 16547N1b	16 58 16''803 \pm 0''02	−42 52 01''42 \pm 0''01	1013 \pm 60	628 \pm 40	96 \pm 5	12.3 \pm 0.6	57.5 \pm 3	2.2 (50 K)
IRAS 16547N2	16 58 17''593 \pm 0''05	−42 51 58''89 \pm 0''05	1540 \pm 140	1390 \pm 130	97 \pm 40	2.0 \pm 0.2	29.0 \pm 3	1.1 (50 K)
IRAS 16547-E	16 58 17''217 \pm 0''02	−42 52 07''46 \pm 0''02	862 \pm 65	532 \pm 47	174 \pm 10	174 \pm 9.0	637 \pm 42	6.1 (150 K)
IRAS 16547-W	16 58 17''062 \pm 0''10	−42 52 07''03 \pm 0''04	2490 \pm 250	1000 \pm 100	77 \pm 4	35.0 \pm 3	535 \pm 52	5.1 (150 K)
IRAS 16547S	16 58 17''535 \pm 0''05	−42 52 15''64 \pm 0''04	958 \pm 153	533 \pm 104	53 \pm 10	4.0 \pm 0.5	16.0 \pm 2	0.23 (50 K)

Note. These physical parameters were obtained with the CASA IMFIT task. In the mass estimation, we have also included which dust temperature was used for a such purpose.

and cannot separate the thermal dust and free-free emission at these millimeter wavelengths arising from IRAS 16547-E and IRAS 16547-W; see, for example, the observations at a wavelength of 3 mm from K. E. I. Tanaka et al. (2020), where they separate both emissions. However, the free-free emission related to this object and at these wavelengths is indeed very low (3%, arising from IRAS 16547-E) as discussed in L. A. Zapata et al. (2019). We capture the dusty envelope surrounding the massive protostars. This dusty and large envelope, with spatial scales that reach $\sim 10,000$ au, has a biconical structure with the open angles that follow the same orientation as that of the radio thermal jet. The morphology of the dusty envelope could be explained in terms of the NW–SE outflow carving or cleaning up the dust and gas in these northern/southern orientations. The rest of the millimeter continuum sources presented in Table 1 could also be part of this biconical envelope although we may be missing some more extended continuum millimeter emission that connects all these structures.

At this millimeter wavelength regime, we can estimate the mass of the sources detected in this work, assuming that the emission is optically thin and isothermal and following the

expression (R. H. Hildebrand 1983)

$$M_d = \frac{D^2 S_\nu}{\kappa_\nu B_\nu(T_d)}, \quad (1)$$

where D is the distance to IRAS 16547–4247, 2.9 ± 0.6 kpc (L. F. Rodríguez et al. 2008); S_ν is the flux density; $\kappa_\nu = 0.0103 \text{ cm}^2 \text{ g}^{-1}$ is the dust mass opacity for a gas-to-dust ratio of 100 appropriate for 1.2 mm (V. Ossenkopf & T. Henning 1994); and $B_\nu(T_d)$ is the Planck function for dust temperature T_d . We considered the Rayleigh–Jeans regime, given the observing frequency, 250 GHz. The estimated values for the mass are given in Table 1. Here, we are assuming a dust temperature $T_d = 150$ K for IRAS 16547-E and IRAS 16547-W, given that they are associated with hot molecular gas (L. A. Zapata et al. 2019; K. E. I. Tanaka et al. 2020), but for the rest sources, we assume $T_d = 50$ K (this a good approximation, as, for example, IRAS 16547-W is associated with a massive protostar). The mass values for IRAS 16547-E and IRAS 16547-W are in very good agreement with those values obtained by L. A. Zapata et al. (2015). Given the uncertainty in

the dust temperature and the opacity, the uncertainty in the mass estimation could be very large, a factor of up to 3 or 4. Using two ellipsoidal Gaussian fitting to the central biconical envelope (Figure 1), we obtain a flux density of 2.2 ± 0.2 Jy and a peak flux of 201 ± 18 mJy beam⁻¹, which corresponds to a total mass of $220 M_{\odot}$, assuming a dust temperature of 16 K, a temperature obtained from the HN^{13}C spectral line (see Section 3.2). Following V. Hernández-Hernández et al. (2014), we estimate a column density of 4.0×10^{26} cm⁻² and a volumetric density of 2.2×10^8 cm⁻³.

The magnetic fields follow the structure of the continuum emission very well. Some of these vectors seem to converge to IRAS 16547-E and IRAS 16547-W, the massive protostars (see Figure 1). A possible explanation is that we are seeing a dusty shell and that the magnetic fields mapped here are part of the envelope opened by the radio thermal jet. Infalling dusty envelopes have also been proposed to explain the orientation of the magnetic fields (see IRAS 18089–1732, P. Sanhueza et al. 2021, and W51, P. M. Koch et al. 2022); however, here we only leave this as a speculative possibility.

The polarized intensity and polarization fraction from IRAS 16547–4247 are presented in Figure 2. The polarized fraction shows more or less a constant intensity toward the edges of the dusty biconical envelope with a substantial increase close to IRAS 16547-E, on its southern side. On the other hand, the polarized fraction shows a structure contrary to the polarized intensity with a depression of the intensity in the central part and the brightest intensity in the edges of the dusty envelope, indicating that the major polarized radiation is coming from the densest parts of the dusty envelope.

The moment 0 (integrated intensity) and moment 1 (intensity-weighted velocity image) maps of the $\text{H}^{13}\text{CO}^+(3-2)$ emission overlaid with the polarization vectors that are tracing the magnetic fields in IRAS 16547–4247, the continuum emission at 1.2 mm, and the thermal free-free jet is presented in Figure 3. To compute these moment maps, we integrate over radial velocities from -40.9 to -15.9 km s⁻¹. The systemic cloud velocity of IRAS 16547–4247 is about -30 km s⁻¹ (K. E. I. Tanaka et al. 2020). These moments show us that the molecular thermal emission is again tracing an envelope with biconical outflow cavities but with some clear bow shocks and outflow cavities far from the dusty envelope, and they coincide well with the north-south free-free thermal jet. These bow-shock structures or outflow cavities are also seen in the millimeter wavelength CH_3OH emission maps from A. E. Higuchi et al. (2015) and are interpreted as part of the outflow emanating from here. From the southernmost bow shock there is a clear correspondence with the compact source called IRAS 16547S (Table 1), which shows polarization. This 1.2 mm continuum source additionally coincides well with the thermal free-free jet on its southern side. The polarization vectors are tracing also a bow shock or outflow cavity structure with a similar orientation to the one traced by the $\text{H}^{13}\text{CO}^+(3-2)$ emission. Perhaps they are part of the bow shock. As mentioned earlier, in this image we also include the moment 1 map that traces the radial velocity field of the region. There is a mix of radial velocities, some molecular arcs are blueshifted, and others are redshifted on both sides of the bipolar thermal free-free jet, likely because of the multiple ejections. The magnetic field vectors are associated with blueshifted and redshifted radial velocities in the inner part of the biconical envelope. There is no distinction between radial velocities.

Figure 4 is similar to Figure 3, but now we present the emission from the $\text{HN}^{13}\text{C}(3-2)$ that is also an optically thin line transition.

In this figure, we include the moment 0 (integrated intensity) and Moment 1 (intensity-weighted velocity image) maps of the molecular emission overlaid with the polarization vectors that are tracing the magnetic fields in IRAS 16547–4247, the continuum emission at 1.2 mm, and the thermal free-free jet, as before. To compute these moment maps, we integrate over radial velocities from -49.7 to -11.3 km s⁻¹. We integrate in a smaller velocity window because the line width for $\text{HN}^{13}\text{C}(3-2)$ line is narrower compared with the $\text{H}^{13}\text{CO}^+(3-2)$ line. From these moments, the molecular thermal emission is tracing again the envelope with biconical outflow cavities observed in the $\text{H}^{13}\text{CO}^+(3-2)$ line and the 1.2 mm continuum emission. However, the emission from the $\text{HN}^{13}\text{C}(3-2)$ is much more compact and is totally related to the 1.2 mm continuum emission. From this spectral line, it is much easier to see the radial velocity field in the innermost part of IRAS 16547–4247. There is a clear velocity gradient from southeast to northwest, with the blueshifted velocities toward the east and the redshifted velocities localized in the northwest. We remark that this gradient was also noted in L. A. Zapata et al. (2015) and was interpreted to be produced by the thermal (free-free) jet emerging from this object. The large velocity gradient (about 20 km s⁻¹) could be associated with the outflow.

In Figure 5, we present the moment 8 and 1 maps (maximum value of the spectrum and radial velocity fields, respectively) of the CS(5–4) molecular emission present in our spectral setup. Additionally, we also include in this figure the continuum emission at 1.2 mm and the thermal NS free-free thermal jet. To compute these moment maps, we integrate over radial velocities from -64.4 to $+9.64$ km s⁻¹. The broader velocity range compared to the other two spectral lines is likely due to the CS tracing more clearly the outflows in the region. From this image, it is easy to see the different ejections from the bipolar thermal jet, and perhaps from other outflows located in the region. A. E. Higuchi et al. (2015) proposed the existence of two more high-velocity CO outflows whose driving sources are located within the dust continuum peak. The orientation of these extra CO outflows do not seem to coincide with that of the wide-angle, large-scale, bipolar outflow detected with APEX (G. Garay et al. 2007) nor the thermal free-free jet (L. F. Rodríguez et al. 2008). These CO outflows could explain the different ejections observed in Figure 5. A second possibility is that the NW-SE bipolar outflow has a strong precession as observed by K. J. Brooks et al. (2003) and L. F. Rodríguez et al. (2008). From Figure 5, the thermal free-free jet should precessing more than 150° (see the aperture angles) on the plane of the sky. Maybe the massive binary systems IRAS 16547-Ea and IRAS 16547-Eb are responsible for this large precession.

Finally, a channel velocity map of the CS(5–4) molecular emission is presented in Figure 6. This image reveals the complex outflow zone in IRAS 16547–4247. This map reveals the structure and radial velocities of every bow shock and outflow cavity present in Figure 5. In particular, the bow shocks and outflow cavities located toward south and north are blue-/redshifted, with not a clear difference on both sides. This can be explained if the precession is occurring far from the plane of the sky, with the ejections having receded and approaching radial velocities toward the south and north sides. Precession in outflows from massive protostars seems to be fairly common. L. A. Zapata et al. (2013), M. T. Beltrán et al. (2016), and C. Goddi et al. (2020) proposed this physical mechanism in W51 North, Cepheus A East, and G31.41+0.31, respectively, to explain the different powerful mass ejections.

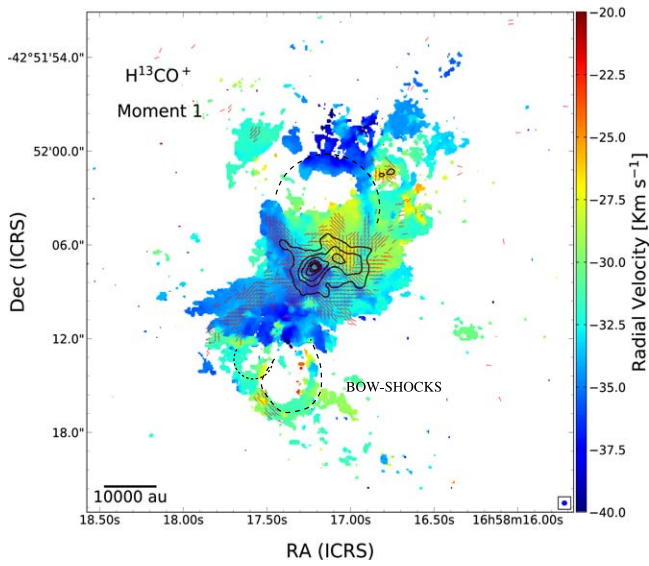
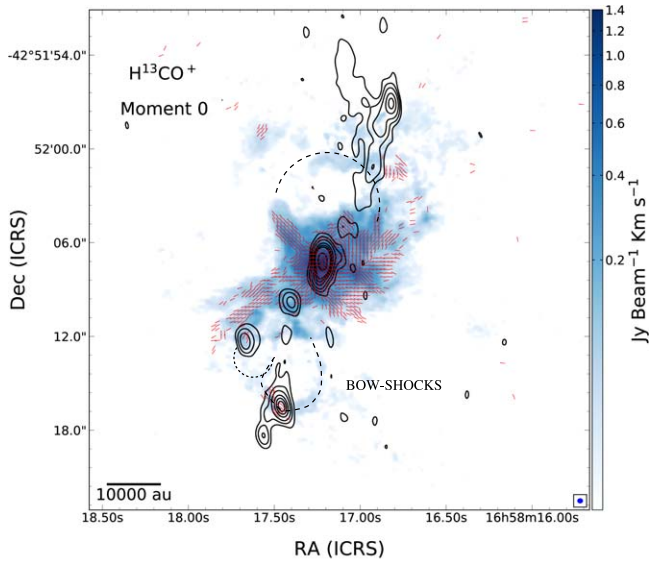


Figure 3. ALMA magnetic field vectors overlaid onto the resulting $\text{H}^{13}\text{CO}^+(3-2)$ line moment 0 (upper) and moment 1 maps (lower) from IRAS 16547–4247. The red vector segments trace the polarization percentage. The vector segment is displayed more or less per every beam, using only data with a 2σ cut in the debiasing process (same as Figure 1). In the upper panel, the black contours are from $-5, 5, 10, 20, 40, 60, 80,$ and 180 times the rms noise of the VLA 3.6 cm continuum emission, which is $20 \mu\text{Jy beam}^{-1}$. The 3.6 cm continuum emission delineates a radio free-free jet with NW–SE orientation reported by G. Garay et al. (2003) and L. F. Rodríguez et al. (2008). The scale bar on the right represents the peak flux of the ALMA $\text{H}^{13}\text{CO}^+(3-2)$ line emission. In the lower panel, the black contours are from $-0.5, 0.5, 1, 5, 10, 20, 40,$ and 60 times $0.2 \text{ mJy beam}^{-1}$ the rms noise of the continuum image. The scale bar on the right represents the the weighted mean radial velocity of the ALMA $\text{H}^{13}\text{CO}^+(3-2)$ line emission. The synthesized beam (half-power contour) of the ALMA line image is shown in the bottom right corner of each panel. The dashed curves trace the multiple bow shocks and outflow cavities discussed in the main text.

3.2. Magnetic Field Strength

In this section, we use the Davis–Chandrasekar–Fermi (DCF; L. J. Davis & J. L. Greenstein 1951; S. Chandrasekhar & E. Fermi 1953) method to estimate the magnetic field strength within some structures that are indicated in Figure 7. The overall morphology of the magnetic field toward IRAS 16547 is complex, but we can observe elongated filament-like structures where the fields are uniform, whereas close to the main two

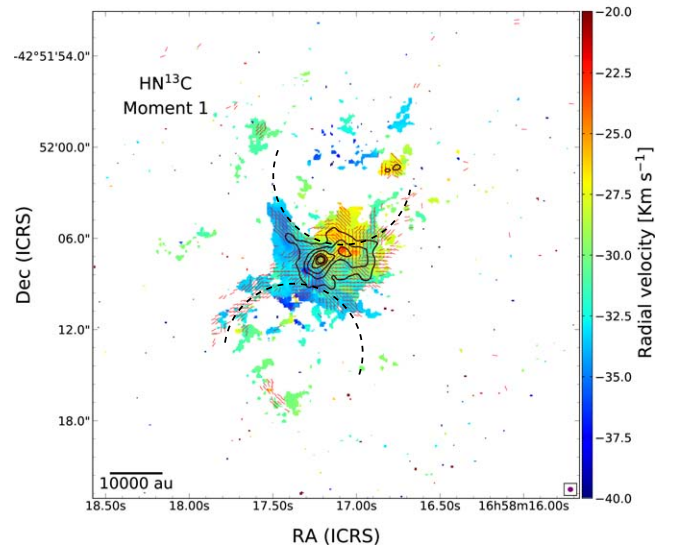
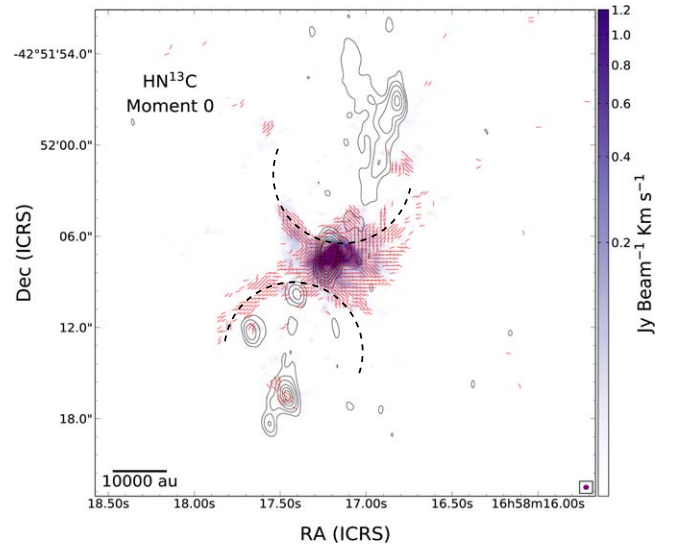


Figure 4. ALMA magnetic field overlaid onto the resulting HN^{13}C line moment 0 (upper) and moment 1 maps (lower) from IRAS 16547–4247. The red vector segments trace the polarization percentage. The vector segment is displayed more or less per every beam, using only data with a 2σ cut in the debiasing process (same as Figure 1). In the upper panel, the black contours are from $-5, 5, 10, 20, 40, 60, 80,$ and 180 times the rms noise of the VLA 3.6 cm continuum emission, which is $20 \mu\text{Jy beam}^{-1}$. The 3.6 cm continuum emission delineates a radio free-free jet with NW–SE orientation reported by G. Garay et al. (2003) and L. F. Rodríguez et al. (2008). The scale bar on the right represents the peak flux of the ALMA HN^{13}C line emission. In the lower panel, the black contours are from $-0.5, 0.5, 1, 5, 10, 20, 40, 60,$ and 80 times $0.2 \text{ mJy beam}^{-1}$ of the ALMA 1.2 mm continuum emission. The scale bar on the right represents the radial velocity of the ALMA HN^{13}C line emission. The synthesized beam (half-power contour) of the ALMA line image is shown in the bottom right corner of each panel. The dashed lines trace more or less the biconical dusty envelope revealed in this study.

protostellar centers, the fields are tangled into an hourglass shape combined with spiral patterns (see Figure 1). The filaments are identified as velocity-coherent structures in at least two different molecular transitions ($\text{CS}(5-4)$ and $\text{HN}^{13}\text{C}(3-2)$) but at the same time avoiding pixels where the magnetic field is very twisted from the main direction (e.g., very close to the protostars) to preserve as much as possible the DCF assumptions. From now on, we focus on the filament-like structures with fairly uniform fields that are also coherent in radial velocity since a model to mimic all this complexity is beyond the scope of this paper and

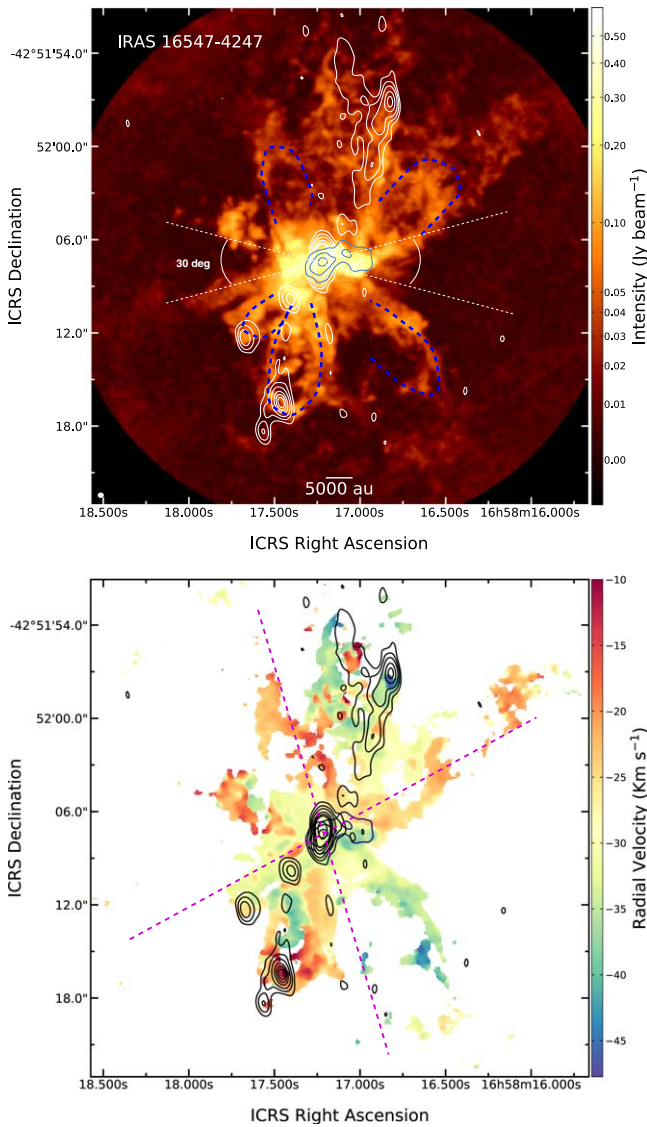


Figure 5. Upper: ALMA moment 8 map of the CS(5–4) from IRAS 16547–4247 overlaid onto the resulting 1.2 mm continuum emission (gray contours) and the VLA 3.6 cm continuum emission (white contours). The gray contours are from 50, 125, and 375 times $0.2 \text{ mJy beam}^{-1}$. The white contours are from $-5, 5, 10, 20, 40, 60, 80,$ and 180 times the rms noise of the VLA 3.6 cm continuum emission, which is $20 \mu\text{Jy beam}^{-1}$. The 3.6 cm continuum emission delineates a radio free–free jet with NW–SE orientation reported by G. Garay et al. (2003) and L. F. Rodríguez et al. (2008). The synthesized beam (half-power contour) of the ALMA continuum image is shown in the bottom right corner. The scale bar on the right represents the peak flux of the ALMA CS line emission. The blue dashed curves trace more or less the multiple bow shocks and outflow cavities revealed by this molecule. The white lines show that aperture angle of the outflow is more than 150° in the north and south sides. Lower: same as the upper image but with the ALMA moment 1 map of the CS(5–4). The scale bar on the right represents the radial velocity of the ALMA CS line emission. The magenta dashed lines mark the orientation of the CO(3–2) outflows reported by A. E. Higuchi et al. (2015).

will be addressed elsewhere. For these filament-like structures, the derivation of the magnetic field strength follows a standard pathway (e.g., M. T. Beltrán et al. 2019; P. Sanhueza et al. 2021), which relies on the expression:

$$B_{\text{pos}} \sim \xi \frac{\sigma_{\text{los}}}{\delta\psi} \sqrt{4\pi\rho}.$$

In this equation, B_{pos} stands for the plane-of-the-sky component of the magnetic field strength, $\xi = 1/2$ is a

correction factor derived from simulations of turbulent clouds (E. C. Ostriker et al. 2001; J. Liu et al. 2021), σ_{los} is the velocity dispersion in the line of sight, $\delta\psi$ is the dispersion of the magnetic field angles, and ρ is the density. Let us make the caveat that there are more appropriate correction factors for cylinders, for instance, in the case of strong magnetic fields $\xi = 0.22$ (J. Liu et al. 2021). Since there is no a priori information on the magnetic fields on this region, we use the classical value for ξ but acknowledge that the field strengths could be a factor of 2 lower only due to geometry issues. The three selected regions appear as distinct dust filaments with a roughly uniform magnetic field orientation aligned along their major axes. The morphology of the polarization segments eases the usage of the DCF method since we can assume a field with constant orientation. We have measurements of dust continuum, polarization angles, and the optically thin gas tracer HN^{13}C covering most of these regions. Each filament-like region comprises more than 40 independent Nyquist-sampled measurements, enough to secure a margin of error $< 3^\circ$ with a 95% reliability.

From Equation (1) and the values presented in Section 3.1, we derive the density (ρ) and the total mass from the dust continuum emission from the three regions shown in Figure 7. We assume that the dust temperature coincides with the gas temperature, which we measure at the position with the maximum brightness of the filaments within the velocity cube. While most of the emission from the filaments is optically thin in all velocity channels ($\tau < 0.2$), the peak emission of the three filaments is marginally optically thick. We use the optically thick maximum emission to estimate the gas temperature, whereas we assume optically thin emission in the filaments to measure the density and mass. The resulting temperature ranges 13–16 K. Using these, the total dust and gas mass enclosed in the filament-like regions amounts to $55\text{--}75 M_\odot$. Assuming a cylindrical volume for each selected region, we find that the density varies between 0.9 and $2.4 \times 10^{-16} \text{ g cm}^{-3}$, which corresponds to number densities between 1.9 and $5.1 \times 10^7 \text{ cm}^{-3}$.

We extract the mean velocity dispersion from the optically thin tracer HN^{13}C after deconvolving with the channel width (0.28 km s^{-1}) and after subtracting in quadrature the thermal component broadening the line, $\sigma_{\text{los}} = \sqrt{\sigma_{\text{observed}}^2 - \sigma_{\text{thermal}}^2}$. The thermal component of the lines is derived using $\sigma_{\text{thermal}} = \sqrt{(K_B T)/(\mu m_H)}$, where K_B is the Boltzmann constant, m_H is the atomic hydrogen weight, T is the temperature of the gas, and $\mu = 28.350$ is the weight of the HN^{13}C molecule. At 16 K, σ_{thermal} takes the value of 0.07 km s^{-1} .

We estimate the magnetic field strength in three different regions extracted from the IRAS 16547 field of view. These regions were selected because the magnetic field orientations were quite uniform within them, which eases the usage of the DCF method. We have measurements of dust continuum, polarization angles, and the optically thin gas tracer HN^{13}C covering the entirety of these regions, which allows us to estimate the magnetic field strength. The average effective radius of the three regions ($r_{\text{eff}} = \sqrt{A/\pi}$, where A is the area) is $0''.68$, or about 2000 au , at the adopted source distance. The smallest of these regions surrounds 1000 au centered at the position of the main continuum sources; we removed it from the average values reported below. This way, we can have an idea of the magnetic field strength at different distances from the source center and at a range of densities.

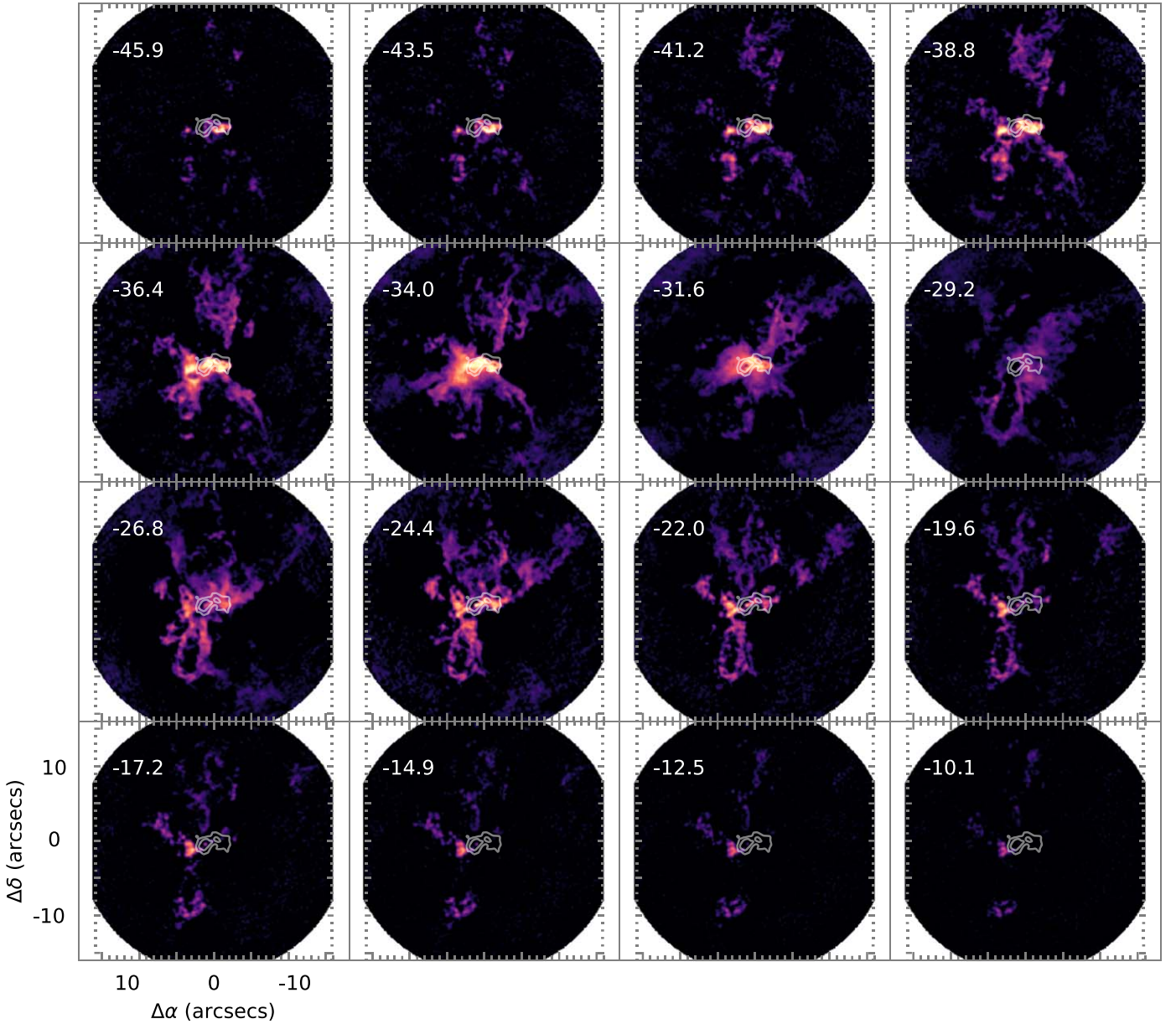


Figure 6. ALMA velocity channel map of the CS(5–4) from IRAS 16547–4247 overlaid onto the resulting 1.2 mm continuum emission (white contours). The white contours are from 50, 125, and 375 times $0.2 \text{ mJy beam}^{-1}$ the rms noise of the image. The synthesized beam (half-power contour) of the ALMA continuum image is $0''.36 \times 0''.32$ and a PA of -88° . The radial velocity is indicated on the upper left side of each channel in kilometers per second.

Likewise, to derive the dispersion of the magnetic field angles ($\delta\psi$), we subtract in quadrature the mean angle uncertainty of the measurements ($\delta\psi_{\text{obs}}$) to the standard deviation of the polarization angles (σ_ψ) found for every specific region: $\delta\psi = \sqrt{\sigma_\psi^2 - \delta\psi_{\text{obs}}^2}$. σ_ψ , the intrinsic angle dispersion, is estimated as the standard deviation of the polarization angles in each region, under the uniform magnetic field assumption. The mean value of $\delta\psi_{\text{obs}}$ (derived as $0.5 \sigma_{QU} / \sqrt{Q^2 + U^2}$ on a pixel-by-pixel basis, with σ_{QU} the noise of the Stokes Q and U images) is $7^\circ.6$, within the three regions considered.

The derived mean magnetic field strength in the regions goes from 2.0 to 6.1 mG, and the Alfvén speed, given by $v_A = B / \sqrt{4\pi\rho}$, from 0.5 to 1.1 km s^{-1} . From here, we extracted the ratio between the turbulent and the magnetic energies: $E_{\text{turb}}/E_{\text{mag}} = 3\sigma_{\text{los}}^2/v_A$. We obtain values between 0.1

and 0.4, suggesting that the magnetic energy would be larger than the turbulence in these filaments (Table 2). Given the high uncertainty dominated by the finite spectral resolution (which dominates the error propagation in the B field strength measurements, $\approx 0.4\text{--}0.7 \text{ mG}$) and the mass estimate (which adds at least another 25% uncertainty), the values of these three quantities (B_{pos} , v_A , and $E_{\text{turb}}/E_{\text{mag}}$) have to be used with extreme caution.

4. Summary

We presented high angular resolution ($\sim 0''.4$), sensitive 1.2 mm dust polarization, and molecular line (HN $^{13}\text{C}(3-2)$, CS(5–4), and H $^{13}\text{CO}^+(3-2)$) ALMA observations of the rotating, and massive hot molecular core embedded in the high-mass star-forming region IRAS 16547–4247. The main conclusions of this study are as follows.

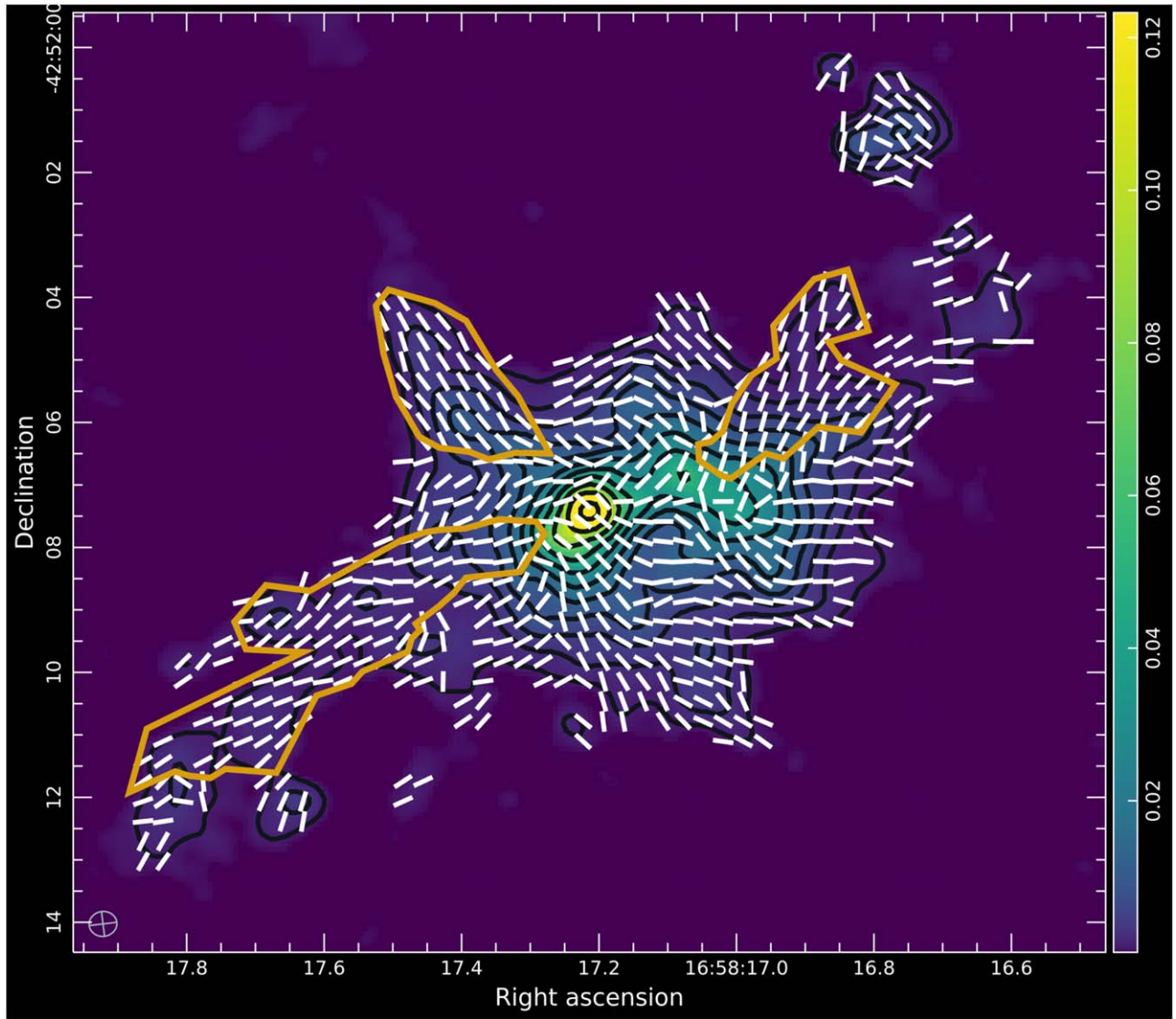


Figure 7. Stokes I continuum image toward the IRAS 16547 region (contours and color scales), overlaid with magnetic field orientation sticks (white segments) and the three filament-like regions (yellow polygons) analyzed in Section 3.2 to derive an order of magnitude for the strength of the magnetic fields. The synthesized beam (half-power contour) of the ALMA continuum image is shown in the bottom left corner. The scale bar on the right represents the peak flux of the ALMA continuum emission.

Table 2
Filament-like Regions Used to Derive the Magnetic Field Strength B_{pos} from the HN^{13}C Observations Using the DCF Method.

ID	$L_{\text{cyl}}^{\text{a}}$ (arcsec)	$r_{\text{cyl}}^{\text{a}}$ (arcsec)	T ($10^{-17} \text{ g cm}^{-3}$)	M (10^6 cm^{-3})	$n_{\text{H}_2}^{\text{b}}$ (km s^{-1})	σ_{los} (deg)	$\delta\Psi$ (mG)	B_{pos} (km s^{-1})	v_{A}	$E_{\text{turb}}/E_{\text{mag}}$
North	7.4	0.40	16	15	1.89	0.26	15.3	2.3	0.7	0.2
East	3.2	0.65	13–16	23–31	3.3–4.4	0.23	10.1	2.0–2.4	0.5	0.4
West	4.4	0.45	13–16	20–27	3.8–5.1	0.21	8.8	5.2–6.1	1.1	0.1

Notes.

^a L_{cyl} and r_{cyl} are the approximate length and radius of the filament-like structures.

^b The density is estimated under the assumption that the 3D morphology of these regions is cylindrical and use two different dust temperature values for the east and west filaments; hence, there are two values for Columns (4), (5), (6), and (9). For Columns (8) and (11), the derived values using both temperatures coincide taking into account the uncertainties, and only one value is provided.

1. In the 1.2 mm continuum Stokes I emission, we reveal a dusty envelope surrounding the massive protostars, IRAS 16547-E and IRAS 16547-W, with dimensions of 10,000 au. This envelope has a biconical structure likely carved by the powerful thermal radio jet present in region. We estimated a

mass and volumetric density for the biconical envelope of $220 M_{\odot}$ and $2 \times 10^8 \text{ cm}^{-3}$, respectively.

2. We report the magnetic field orientations of the biconical envelope in IRAS 16547–4247. The magnetic fields vectors follow very well the structure of the continuum emission or

the biconical envelope. Some of these vectors seem to converge to IRAS 16547-E and IRAS 16547-W, the massive protostars. Some these polarization vectors likely are tracing the cavities of the outflows reported in the region. However, some of them could also be tracing infall material, but more observations are need to confirm this possibility.

3. The velocity fields revealed by the optically thin spectral lines (e.g., HN^{13}C) showed velocity gradients with a good correspondence with the magnetic fields.
4. The CS(5–4) molecular line emission reveals multiple ejections with different orientations; some of them seem to follow the NW–SE radio thermal jet. All these ejections could be explained if the binary massive system in the middle of IRAS 16547–4247 is precessing strongly, causing the motion of the bipolar outflow.
5. We derived a magnetic field strength in the regions that goes from 2 to 6.1 mG (the latter found to be associated to the central source position).

Acknowledgments

We thank the anonymous referee for providing a constructive report, which indeed improved the paper. This paper makes use of the following ALMA data: ADS/JAO.ALMA#2017.1.00101.S ALMA is a partnership of ESO (representing its member states), NSF (USA) and NINS (Japan), together with NRC (Canada), MOST and ASIAA (Taiwan), and KASI (Republic of Korea), in cooperation with the Republic of Chile. The Joint ALMA Observatory is operated by ESO, AUI/NRAO and NAOJ. L.A.Z. acknowledges financial support from CONACyT-280775, UNAM-PAPIIT IN110618, and IN112323 grants, México. L.F.R. acknowledges the financial support of DGAPA (UNAM) IN105617, IN101418, IN110618 and IN112417 and CONACyT 238631 and 280775-CF. grant 263356. P.S. was partially supported by a Grant-in-Aid for Scientific Research (KAKENHI numbers JP22H01271 and JP24K17100) of the Japan Society for the Promotion of Science (JSPS). Y.C. was partially supported by a Grant-in-Aid for Scientific Research (KAKENHI number JP24K17103) of the JSPS. M.T.B. acknowledges financial support through the INAF Large Grant *The role of MAGnetic fields in MAssive star formation* (MAGMA). K.P. is a Royal Society University Research Fellow, supported by grant No. URF R1 211322. M.F.L. acknowledges support from the European Research Executive Agency HORIZON-MSCA-2021-SE-01 Research and Innovation program under the Marie Skłodowska-Curie grant agreement No. 101086388 (LACEGAL). M.F.L. also acknowledges the warmth and hospitality of the ICE-UB group of star formation.

Facility: ALMA.

Software: CASA (CASA Team et al. 2022).

ORCID iDs

Luis A. Zapata <https://orcid.org/0000-0003-2343-7937>
 Manuel Fernández-López <https://orcid.org/0000-0001-5811-0454>
 Patricio Sanhueza <https://orcid.org/0000-0002-7125-7685>
 Josep M. Girart <https://orcid.org/0000-0002-3829-5591>
 Luis F. Rodríguez <https://orcid.org/0000-0003-2737-5681>
 Paulo Cortés <https://orcid.org/0000-0002-3583-780X>
 Patrick Koch <https://orcid.org/0000-0003-2777-5861>
 Maria T. Beltrán <https://orcid.org/0000-0003-3315-5626>
 Kate Pattle <https://orcid.org/0000-0002-8557-3582>

Henrik Beuther <https://orcid.org/0000-0002-1700-090X>
 Piyali Saha <https://orcid.org/0000-0002-0028-1354>
 Wenyu Jiao <https://orcid.org/0000-0001-9822-7817>
 Fengwei Xu <https://orcid.org/0000-0001-5950-1932>
 Xing Walker Lu <https://orcid.org/0000-0003-2619-9305>
 Fernando Olguin <https://orcid.org/0000-0002-0331-5708>
 Shanghuo Li <https://orcid.org/0000-0003-1275-5251>
 Ian W. Stephens <https://orcid.org/0000-0003-3017-4418>
 Ji-hyun Kang <https://orcid.org/0000-0001-7379-6263>
 Yu Cheng <https://orcid.org/0000-0002-8691-4588>
 Spandan Choudhury <https://orcid.org/0000-0002-7497-2713>
 Kaho Morii <https://orcid.org/0000-0002-6752-6061>
 Eun Jung Chung <https://orcid.org/0000-0003-0014-1527>
 Jia-Wei Wang <https://orcid.org/0000-0002-6668-974X>
 Jihye Hwang <https://orcid.org/0000-0001-7866-2686>
 A-Ran Lyo <https://orcid.org/0000-0002-9907-8427>
 Q. Zhang <https://orcid.org/0000-0003-2384-6589>
 Huei-Ru Vivien Chen <https://orcid.org/0000-0002-9774-1846>

References

- Beltrán, M. T., Cesaroni, R., Moscadelli, L., et al. 2016, *A&A*, 593, A49
 Beltrán, M. T., Padovani, M., Girart, J. M., et al. 2019, *A&A*, 630, A54
 Beuther, H., Soler, J. D., Linz, H., et al. 2020, *ApJ*, 904, 168
 Blandford, R. D., & Payne, D. G. 1982, *MNRAS*, 199, 883
 Brooks, K. J., Garay, G., Mardones, D., & Bronfman, L. 2003, *ApJL*, 594, L131
 CASA Team, Bean, B., Bhatnagar, S., et al. 2022, *PASP*, 134, 114501
 Chandrasekhar, S., & Fermi, E. 1953, *ApJ*, 118, 116
 Cortés, P. C., Girart, J. M., Sanhueza, P., et al. 2024, *ApJ*, 972, 115
 Cortés, P. C., Sanhueza, P., Houde, M., et al. 2021, *ApJ*, 923, 204
 Davis, L. J., & Greenstein, J. L. 1951, *ApJ*, 114, 206
 de Valon, A., Dougados, C., Cabrit, S., et al. 2020, *A&A*, 634, L12
 Fernández-López, M., Sanhueza, P., Zapata, L. A., et al. 2021, *ApJ*, 913, 29
 Franco-Hernández, R., Moran, J. M., Rodríguez, L. F., & Garay, G. 2009, *ApJ*, 701, 974
 Garay, G., Brooks, K. J., Mardones, D., & Norris, R. P. 2003, *ApJ*, 587, 739
 Garay, G., Mardones, D., Bronfman, L., et al. 2007, *A&A*, 463, 217
 Goddi, C., Ginsburg, A., Maud, L. T., Zhang, Q., & Zapata, L. A. 2020, *ApJ*, 905, 25
 Hernández-Hernández, V., Zapata, L., Kurtz, S., & Garay, G. 2014, *ApJ*, 786, 38
 Higuchi, A. E., Saigo, K., Chibueze, J. O., et al. 2015, *ApJL*, 798, L33
 Hildebrand, R. H. 1983, *QJRAS*, 24, 267
 Hoang, T., & Lazarian, A. 2008, *MNRAS*, 388, 117
 Hull, C. L. H., & Zhang, Q. 2019, *FrASS*, 6, 3
 Koch, P. M., Tang, Y.-W., Ho, P. T. P., et al. 2022, *ApJ*, 940, 89
 Launhardt, R., Pavlyuchenkov, Y. N., Akimkin, V. V., et al. 2023, *A&A*, 678, A135
 Lee, C.-F., Ho, P. T. P., Li, Z.-Y., et al. 2017, *NatAs*, 1, 0152
 Liu, J., Zhang, Q., Commerçon, B., et al. 2021, *ApJ*, 919, 79
 Liu, J., Zhang, Q., Qiu, K., et al. 2020, *ApJ*, 895, 142
 Liu, J., Zhang, Q., Koch, P. M., et al. 2023, *ApJ*, 945, 160
 López-Vázquez, J. A., Zapata, L. A., & Lee, C.-F. 2023, *ApJ*, 944, 63
 Ossenkopf, V., & Henning, T. 1994, *A&A*, 291, 943
 Ostriker, E. C., Stone, J. M., & Gammie, C. F. 2001, *ApJ*, 546, 980
 Palau, A., Zhang, Q., Girart, J. M., et al. 2021, *ApJ*, 912, 159
 Pattle, K., Fissel, L., Tahani, M., Liu, T., & Ntormousi, E. 2023, in ASP Conf. Ser. 534, Protostars and Planets VII, ed. S. Inutsuka et al. (San Francisco, CA: ASP), 193
 Rodríguez, L. F., González, R. F., Raga, A. C., et al. 2012, *A&A*, 537, A123
 Rodríguez, L. F., Moran, J. M., Franco-Hernández, R., et al. 2008, *AJ*, 135, 2370
 Saha, P., Sanhueza, P., Padovani, M., et al. 2024, *ApJL*, 972, L6
 Sanhueza, P., Garay, G., Bronfman, L., et al. 2010, *ApJ*, 715, 18
 Sanhueza, P., Girart, J. M., Padovani, M., et al. 2021, *ApJL*, 915, L10
 Tanaka, K. E. I., Zhang, Y., Hirota, T., et al. 2020, *ApJL*, 900, L2
 Zapata, L. A., Fernández-López, M., Curiel, S., Patel, N., & Rodríguez, L. F. 2013, arXiv:1305.4084
 Zapata, L. A., Fernández-López, M., Leurini, S., et al. 2023, *ApJL*, 956, L35
 Zapata, L. A., Garay, G., Palau, A., et al. 2019, *ApJ*, 872, 176
 Zapata, L. A., Palau, A., Galván-Madrid, R., et al. 2015, *MNRAS*, 447, 1826